Journal of Energy Storage 152 (2026) 120653

Contents lists available at ScienceDirect

Journal of Energy Storage

journal homepage: www.elsevier.com/locate/est

Research papers

Degradation of $LiFePO_4$ batteries after a real hybrid-bus extended application: Investigation of ageing phenomena and heterogeneity of performance

G. Sordi [a,b,c,*], G.M. Trippetta [a,d], D. Luder [b,c], S. Berg [c,e], W. Li [b,c], E. Figgemeier [b,c,e], D.U. Sauer [b,c,e], A. Casalegno [a], C. Rabissi [a,**]

[a] Politecnico di Milano, Department of Energy, via Lambruschini 4, 20156, Milano, Italy
[b] Institute for Power Electronics and Electrical Drives (ISEA), RWTH Aachen University, 52074, Aachen, Germany
[c] Center for Ageing, Reliability and Lifetime Prediction of Electrochemical and Power Electronic Systems (CARL), RWTH Aachen University, 52074, Aachen, Germany
[d] Applied Electrochemistry, Department of Chemical Engineering, KTH Royal Institute of Technology, SE-100 44, Stockholm, Sweden
[e] Helmholtz Institute Münster (HI MS), Forschungszentrum Jülich, Jülich, Germany

ARTICLE INFO

Keywords:
Lithium-ion battery
LFP
Degradation
Diagnostics
Real-world
Heterogeneity

ABSTRACT

Li-ion battery rapidly emerged as a key enabling technology towards the widespread adoption of low and zero-emissions vehicles. However, the understanding of long-term degradation still requires consolidation due to the complex interplay of several ageing mechanisms. Furthermore, it is widely reported in the literature that major differences could occur between laboratory-induced and real-world degradation. Hence, this work analyses a batch of 24 LFP cells aged in a hybrid-bus application for up to 8 years. The combined use of a selection of experimental measurements, ex-situ investigations and physical model simulations is the proposed tool to quantify the performance decay, identify the most important degradation mechanism, assess the heterogeneity among cells and relate it with the operating conditions. The characterisation showed significant heterogeneity in residual capacity (from 80% down to 55% with respect to BoL) and impedance, suggesting an uneven module cooling effectiveness. Electrolyte degradation, generating together with Solid-electrolyte interface (SEI) growth a passivation and precipitation layer on the negative electrode surface, is identified as the dominant degradation mechanism, leading to a large loss of both lithium inventory and electrolyte conductivity, as suggested by modelling analyses and confirmed with ex-situ investigations. This work provides novel insights into the state of health of a spent lithium-ion battery from the field as preliminary activity towards battery second life.

1. Introduction

Li-ion battery technology features an unmatched combination of high energy and power density at a reasonably low cost, making it the technology of choice for portable electronics, power tools, and hybrid/full electric vehicles [1–3]. As a result, Li-ion batteries are of prior interest from both industry and government funding agencies, and research in this field has abounded in recent years [4,5].

However, several aspects are still to be improved to further increase technology competitiveness. One of them is ageing, occurring with the operation. Such degradation is the complex result of the interplay of several physicochemical mechanisms, which affect all the different components of the cells, including electrodes, electrolytes, separators, and current collectors [6,7]. The consolidation of physical and chemical mechanisms interplaying behind cell degradation is still an open issue for both research and the industrial world, as well as their identifiability [8,9]. One relevant consequence is the complex evaluation of the suitability of spent batteries to the so-called “second-life”, namely its utilisation in a different sector, like energy storage, after the “first life”, like the usage in the automotive sector.

Among several chemistries available, Lithium-iron phosphate (LFP) is a very popular one adopted at positive electrode, thanks to the high thermal stability and power capabilities. Their main drawback is associated with the limited energy density since LFP shows a lower electric

* Corresponding author at: Politecnico di Milano, Department of Energy, via Lambruschini 4, 20156, Milano, Italy.
** Corresponding author.
E-mail addresses: gabriele.sordi@polimi.it (G. Sordi), claudio.rabissi@polimi.it (C. Rabissi).

https://doi.org/10.1016/j.est.2026.120653
Received 9 June 2025; Received in revised form 5 December 2025; Accepted 15 January 2026
Available online 29 January 2026

potential compared to layered oxide materials [3]. Accordingly, several works have investigated its characteristics. Among them, degradation and durability are important topics to widen their application. For instance, Li et al. [10] studied the behaviour of LFP batteries during storage at 20 °C, 40 °C and 60 °C for more than 7000 h. They noticed a significant lithium loss that was associated with SEI formation/growth. However, at elevated temperatures, iron ions from the LFP structure might dissolve, migrate in the electrolyte and precipitate on the surface of the negative electrode. Such an effect can cause an increase in SEI growth since conductive iron favours electron transport and blockage of active sites of graphite, thus inhibiting the lithiation of the electrode. In a subsequent work [11], they cycled some cells at the same temperatures to understand the additional loss of performance due to the usage. In this case, they identified a loss of usable active material on the graphite electrode, promoted by high temperatures and currents.

Groot et al. [12] cycled LFP cells in 34 different combinations of operating conditions, exploiting constant-current cycles. They observed how the degradation of asymmetrical cycles is different from symmetrical ones, and, in particular, they underlined the role of rest phases at high and low SoC and the detrimental combination of fast charging profiles with slow discharges. Sarasketa-Zabala et al. [13] investigated degradation on LFP batteries undergoing deep discharge with constant current at 30 °C for thousands of cycles. They observed a two-stage behaviour, with a change of slope of the capacity loss and the internal resistance, suggesting a change in the dominant ageing mechanism. The growth of the high-frequency intercept of the impedance was related to the decomposition of the electrolyte. They identified a first linear trend with the loss of lithium inventory (LLI) effect as a major effect and then a parabolic one with a combination of LLI and loss of active material on the negative electrode (LAM_{NE}). After cell opening, they found lithium deposits on very aged samples, which were absent at the beginning and at an intermediate stage of the campaign. Therefore, they related the first stage to a SEI-dominated stage and the second to a lithium-plating-dominated one, where both mechanisms were assumed to be pure LLI-related.

Different diagnostic techniques are employed in the scientific literature. For instance, quasi-equilibrium analysis is often performed to estimate the amount of lithium and active electrode losses. Dubarry and Liaw developed and extensively applied incremental capacity analysis to LFP cells to describe degradation [14,15]. Notably, LFP shows a peculiar open-circuit potential (OCP) curve, with a single plateau around 3.45 V, which lasts until the very extreme lithiation levels [3,16]. Li et al. [17] the differential voltage (DV) analysis on LFP, associating the decrease of the charge exchange of the first plateau of graphite to LLI and the contraction of the second plateau to the loss of active graphite sites. Sarasketa-Zabala et al. [13] exploited different techniques as periodic characterisation tests during their cyclic ageing campaign. They tracked the evolution of residual capacity through constant current charge and discharge of LLI and LAM_{NE} through C/5 cycles, the internal resistance during a pulse and impedance by means of electrochemical impedance spectroscopy. Lastly, Groot et al. [12] monitored the trend of residual capacity, measured through a 1C discharge, and of the impedance by way of electrochemical impedance spectroscopy (EIS).

Post-mortem techniques validate degradation understanding. Li et al. [10] confirmed the presence of iron on graphite due to dissolution with X-ray photoelectron spectroscopy (XPS) analysis and later applied Raman spectroscopy to verify the existence of defects in the graphite structure of cycled electrodes [11]. At the end of the campaign, Sarasketa-Zabala et al. [13] conducted post-mortem analyses exploiting field emission gun-scanning electron microscopy with Energy Dispersive X-ray Spectroscopy (EDS), low C-rate cycling of harvested material in coin cell configuration with lithium counter electrode and X-ray diffraction.

Modelling techniques are typically used to predict capacity loss or resistance increase. Schimpe et al. [18] performed a wide experimental campaign to parametrise a semi-empirical degradation model to predict the capacity loss during storage and cycling at various operating conditions. They identified a squared-root dependency over time for calendar ageing, with an Arrhenius relation with storage temperature and a Tafel equation to take the state of charge into account. They also modelled cycle ageing as the superposition of four terms, namely calendar ageing, cycle ageing at low temperature, cycle ageing at high temperature and cycle ageing at high temperature and high SoC. Lastly, they validated the model against real data from a residential storage application.

As in these works, it is very common to induce degradation in the laboratory, exploiting constant-current cycles due to the large amount of information and the complexity of collecting spent batteries from the field. The same procedure was exploited also in [11,12]. Nevertheless, it has been demonstrated that significant differences can occur between laboratory-induced and real-world degradation [19]. Ramirez-Meyers et al. [20] reported the analysis of used batteries from a hybrid bus application. They evaluated the state of health of the pack by testing different cells by position and measured a wide heterogeneity of performance both as residual capacity and impedance. However, their interest was devoted to the reusability in second-life applications considering the heterogeneity of performance, and they did not perform any degradation analysis.

According to the literature review, comprehensive degradation analysis of real-world LFP battery samples is not commonly available. This study proposes an extensive characterisation of LFP batteries sourced from the field, integrating discharge curve analysis and impedance tests with a suite of ex-situ measurements, such as half-cell cycling, EIS, and advanced imaging techniques. Furthermore, building on previous work by the same authors on a different cell type [21,22], physical models are utilised to simulate the operation of the samples. This involves varying degradation-relevant physical parameters between fresh and aged states to account for the degradation effects on performance. By combining full-cell tests, ex-situ measurements, and modelling simulations, this approach aims to elucidate the mechanisms of performance degradation. Such a combination of long-term field-aged samples and multi-scale experimental and modelling diagnostic techniques has not, to the best of our knowledge, been previously reported for LFP batteries, and it proves essential in this work for quantitatively decoupling degradation mechanisms and explaining the pronounced heterogeneity observed in the field.

It provides a detailed interpretation of ageing by identifying the most likely degradation phenomena, thereby offering a comprehensive understanding of the factors affecting the longevity and efficiency of LFP batteries in real-world applications.

2. Experimental

2.1. Description of the battery samples

The characteristics of the tested samples are listed in Table 1. They have been provided by IVECO Bus with the purpose of assessing the technical feasibility of a second-life utilisation in a privately funded project. It is worth mentioning that the cells belong to two different cell type releases: very aged cells are coded as “M1A”, while fresh or little aged cells are coded as “M1B”. The differences between them are

Table 1
Characteristics of the experimental samples [23,24].

Manufacturer	A123	A123
Model	ANR26650M1A	ANR26650M1B
Nominal capacity	2.3 Ah	2.5 Ah
Operating window	2 V–3.6 V	2 V–3.6 V
Electrode materials	LFP|Graphite	LFP|Graphite
Recommended fast charge [A]	10	10
Continuous max discharge [A]	70	50
Internal impedance @1 kHz [mΩ]	8	6

provided in the table. This information is relevant since it limits the comparability of performance between a fresh M1B cell and an aged M1A one. Since M1A is not available on the market anymore, type M1B are considered as a benchmark of performance for M1A.

It is worth stressing that ex-situ inspection of selected M1A and M1B cells (not reported here for brevity) indicates that the main design differences between the two revisions concern the positive electrode - namely a slightly thinner LFP coating and a longer jelly-roll -, features that are consistent with the change in specifications reported in Table 1. By contrast, the negative electrode architecture appears essentially unchanged, and -considering that ageing in these samples predominantly affects the negative electrode as will be confirmed in the results section - this supports the use of M1B as a suitable pristine reference without significantly affecting the validity of the ageing analysis.

A total of 15 aged modules were available, coming from three hybrid buses of the same type. Due to module replacements, modules were manufactured in different years and, therefore, experienced different operational life on the bus. All three buses worked in France in the public transportation sector.

2.2. Battery pack design

The battery pack is described here to understand the conditions in which the cells operate. In each bus, the battery pack is made of 16 series-connected modules. Each module is constituted by 12 series-connected strings, while each string is a parallel of 8 parallel-connected single cells. Cells are soldered between two aluminium sheets.

The pack is air-cooled with ambient air. As described in Fig. 1a, the air is forced to flow below the modules, passes through and is ejected from the top. Two temperature sensors are placed attached to two cells per module (Fig. 1b). The first measures the surface temperature of one cell positioned in the lower ranks of the module, while the second is positioned in the higher ranks. Air can be heated by means of an electrical resistance if the system works in heating mode.

2.3. Single cell samples selection

In this work, 40 single cells were selected and extracted from their modules. The choice aims to investigate:

- different ages (manufactured in 2013 or 2016)
- different position inside the string
- different amount of warning counts, which are explained in Section 2.5.

Two strings with the same characteristics are evaluated for the purpose of generalizability of the results. The details of these characteristics are provided in Table 2. With respect to the position of the cells inside the string, the colour coding and numbering shown in Fig. 1c are applied to all the cells. Thus, cells with numbers 1 and 2 are located at the outlet section of the cooling air, while 7 and 8 are in the lower ranks of the module, at the inlet of the cooling stream.

2.4. Diagnostic tools and testing equipment

The fresh cells are firstly investigated by performing full discharges, EIS and pulses at various combinations of C-rate, temperature and state of charge. At least two cells underwent the same test for reproducibility purposes, and results show very little variance. Aged cells underwent a selection of tests, as follows:

- one full discharge at C/10, 25 °C
- one full discharge at 1C, 25 °C
- one EIS at 50% SoC, 25 °C (galvanostatic, <10 mV peak-peak, 40 logarithmically-spaced frequencies from 4 kHz to 10mHz).

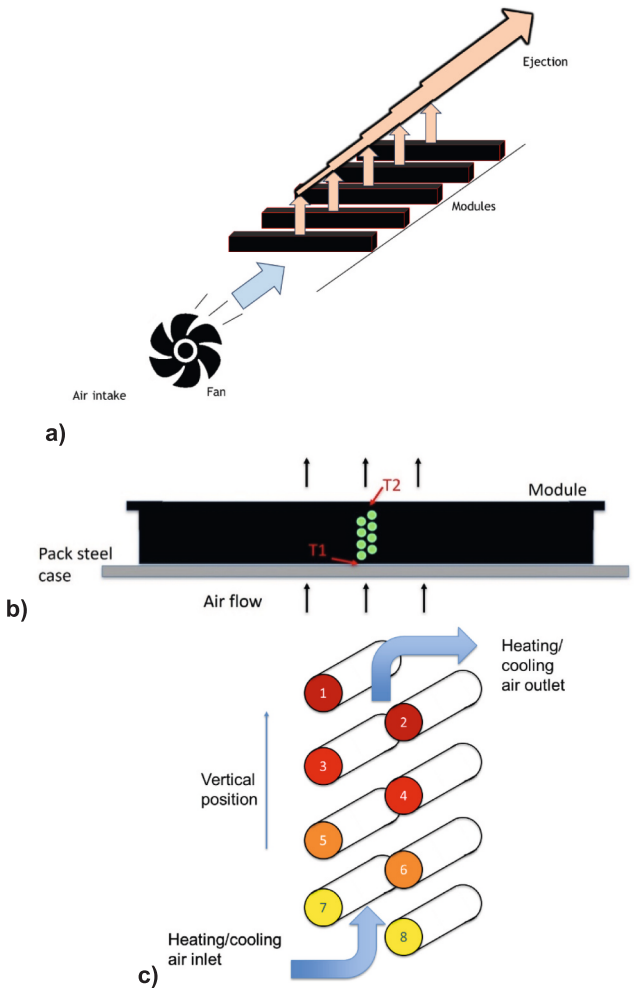

Fig. 1. (a) Scheme of the cooling system. (b) Detail of the air flow passing through one module. One string and the position of the thermistors are highlighted. (c) Colour coding and numbering for cells inside each string.

Table 2
Characteristics of the tested samples.

Code	Module	String	Tested cells	Manufacturing year	Warning count
A0811	8	11	From 1 to 8	2013	Extremely high
A0812	8	12	From 1 to 8	2013	High
A0802	8	2	From 1 to 8	2013	Low
A0605	6	5	1-3-5-7	2013	High
A0602	6	2	1-3-5-7	2013	Low
B0101	1	1	1-3-5-7	2016	0
B0112	1	12	1-3-5-7	2016	0

- Discharges and EIS are performed with a custom-developed experimental testbench [25] testing station, including one power supply and two five-channel electronic loads, resulting in eight independent testing channels, each capable of up to 80 A dynamic charge-discharge testing with EIS capability. All tests are performed in a Binder MKF 720 Eucar VI climatic chamber, with test temperature always referring to the setpoint of the climatic chamber. Sample surface temperature is monitored through type K thermocouples.

2.5. On-board data

The first step of the analysis involves the data collected by the battery management system (BMS) of the vehicles, which were made available. In particular, the distribution of pack current, string and module voltages and temperature were provided. A few insights on the current distribution are reported in S1 of the Supplementary Materials enclosed in this publication.

Temperature is measured as a number of sampled events, discretised into 5 °C bands, for each module. The most frequent measurements of sensor T1 report values in the order of 25 °C to 35 °C. Differences between modules are present, but these modules have different ages due to module replacements along the vehicle lifetime. Thus, it may affect this analysis. More extreme temperatures are seldom recorded but almost never out of the [5 °C; 45 °C] interval. Differently, T2 always records higher temperatures with respect to T1, in the interval 35 °C–40 °C. Therefore, an average difference of 5 °C or larger is estimated between inlet and outlet sections. This persistent gradient, observed over the entire operational life, suggests a systematic difference in long-term thermal exposure across the vertical direction of the module. The temperature measurements for one pack are shown in S2 as heatmaps of both sensors together with the detail of one module.

Lastly, the BMS provides the number of events when the voltage of the strings overcame the voltage cut-offs during operation. This indicator, in the following labelled as "warnings count", is considered in the selection of the cells for the experimental campaign as an early indicator of the state of health.

2.6. Modelling tools

The interpretation of degradation is supported by the use of two physical models to reproduce the operation of the cells under different conditions. First, one equilibrium model is exploited to simulate close-to-equilibrium discharge curves to identify the loss of lithium inventory (LLI) and the loss of active electrodes material (LAM_{NE}, LAM_{PE}). This model, described in supplementary materials, works in a Matlab environment and it is freely available. In the present work, a C/10 full discharge at 25 °C is exploited to approximate equilibrium conditions. Parameters are identified through a Particle Swarm Optimisation (PSO) algorithm, targeting the best fit of the experimental differential voltage curve. The model uses the open-circuit potential (OCP) curves of the electrodes, provided as look-up tables, as input data. Overpotentials are represented by a single, lumped resistance. The stoichiometric operating boundaries of the electrodes are determined using half-cell C/50 cycles in a coin cell configuration for a fresh sample. For aged cells, these boundaries are adapted on the values of LLI and LAMs. A non-linear solver is utilised to align the OCP curves for aged cells, factoring in the LAM values (acting as contraction factors for the curves and implemented as purely delithiated) and the charge balance, which is influenced by LLI. Operating boundaries are later defined as the unique conditions of matching between the OCP curves providing the required voltage cut-offs (upper and lower). For more information on the model description and parameter identification method, the reader is referred to [26].

The pseudo-two-dimensional (P2D) model is later utilised to simulate high C-rate discharge and EIS. The results for the fresh cells are reported in Section 3.3, while the selection of the fitting parameters for aged cells is discussed in Section 3.6. This model is coupled with a thermal model, described in [27], to account for the effects of self-heating. The properties of electrodes and electrolytes are explicitly dependent on temperature.

Overall, LLI and LAM parameters are taken from the q-OCP analysis; the P2D model is calibrated only on a limited set of kinetic and electrolyte-transport parameters required to reproduce high-rate discharge and impedance behaviour.

2.7. Post-mortem analyses

One fresh and one strongly-aged sample is opened in the glovebox to undergo ex-situ investigations. Coin cells are fabricated with harvested material from various positions of the jelly roll, with lithium chips as counter-electrode and abundant amount of fresh electrolyte (90 µL). They are cycled to perform quasi-open circuit potential measurements (q-OCP) at C/50 and 21 °C, exploiting a Neware BTS4000-5V10mA battery testing system, quantifying the residual performance and possible heterogeneities. The voltage cut-offs are selected depending on the material as follows:

- Graphite: between 0.01 V and 1.6 V
- LFP: between 2.8 V and 3.75 V

EIS at 25 °C and different SoCs are also performed. They are performed either by means of a Gamry Reference 3000 or Gamry Interface 5000E potentiostats. All cells are positioned in a thermal chamber (Binder MK 53) and left at rest until thermal equilibrium at 25 °C is reached. Then, they undergo a charge (delithiation) phase up to the maximum voltage selected for the Q-OCP measurements. After 5 h of rest, the following sequence is conducted:

- OCV is measured for 30 s.
- Galvanostatic EIS is performed.
- OCV is measured for 30 s.
- A C/10 discharge (lithiation) is performed for the desired DoD.
- The cell remains at rest for 5 h, to ensure the equilibrium condition for the following EIS.
- The sequence is interrupted when either the cell reaches the minimum voltage threshold during discharge or the expected number of repetitions is achieved. Depth of discharge and C-rate are scaled to the C/50 capacity measured in the Q-OCP estimation. EIS is performed at 5% or 10% SoC intervals. Preliminary tests are performed to determine a suitable current amplitude. The frequency range spans from 20 kHz to 10mHz, with 20 points per decade. 3 sines are performed for every frequency

Lastly, the morphology of the electrodes is investigated through Scanning Electron Microscopy (SEM) images at different magnifications, and EDS is exploited to perform chemical composition analysis. For more information, the reader can consult [28].

3. Results and discussion

3.1. Fresh cell - testing

3.1.1. Discharge test

Fresh cells are investigated to have a benchmark of performance. Full discharges at different temperatures and C-rates are shown in Fig. 2a–b. The cells show very good rate capabilities, releasing more than 96% of the nominal capacity even at 10C, 10 °C. At low rate, the typical shape of LFP|Graphite discharge curve is evident, with the staging behaviour of graphite showing three clear voltage plateaus. These features are lost at high rates, where losses add on top. Surface temperature is measured along the tests. No significant temperature rise is measured at C/10, while an increase within 5 °C can be recorded at the end of discharge at 1C, corresponding to irreversibility of the graphite intercalation reaction. Heat generation becomes non-negligible at 10C, at all temperatures, with an almost linear trend along the discharge.

3.1.2. EIS

EIS at different temperatures and SoCs is also performed and reported in Fig. 2c–f. It shows the usual inductive loop at very high frequencies. Around 1 kHz, the spectrum crosses the x-axis, thus providing the purely resistive response of the device. Between 1 kHz and 10 Hz, the

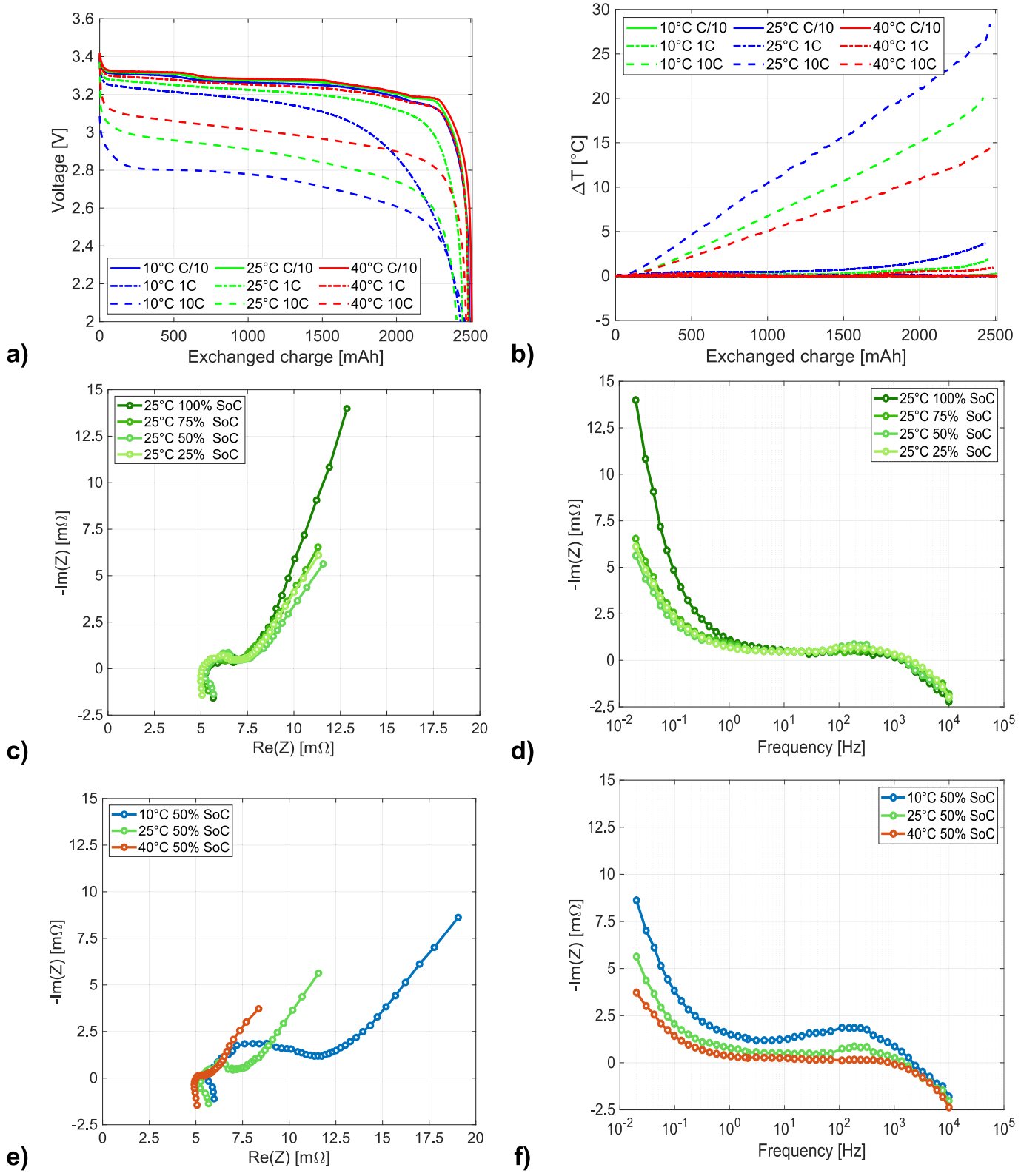

Fig. 2. (a) Full discharges at various temperatures and C-rates for fresh cells. (b) Corresponding temperature rise, measured on the surface of the cells. (c) Nyquist plot and (d) Bode representation of the imaginary part of the EIS of a fresh cell at varying states of charge. (e) Nyquist plot of EIS at different temperatures and (f) corresponding Bode plot of the imaginary component.

spectrum exhibits an elongated semicircle, while at lower frequencies, a linear branch is evident. Variations due to SoC [13] are relatively limited, with the growth of the low-frequency tail at 100% SoC as the most evident effect. On the contrary, temperature affects the size of the impedance greatly. The larger the temperature, the smaller the impedance, especially in the charge-transfer area. Little difference in HFR is detected, while the diffusion tail varies in magnitude but preserves the same slope in the Nyquist plot. No major differences in frequencies are

present.

3.2. Fresh cell – ex-situ analysis

3.2.1. Half-cell Q-OCP

One fresh cell was opened in the glovebox with the procedure described in Section 2.7. q-OCP measurements are reported in Fig. 3, while EIS measurements are presented in Fig. S4 of the Supplementary Materials attached to this manuscript.

In Fig. 3a, the charge (delithiation, blue) and discharge (lithiation, red) curves of one LFP half-cell at C/50 are shown. LFP shows a very flat profile, as known in the literature [3,16]. There is a mismatch as charge count between charge and discharge, probably due to a small self-discharge rate. Moreover, there is a slight hysteresis at the edges, where voltage variations are more or less steep, depending on the phase. Furthermore, between lithiation and delithiation phases, there is a voltage difference, which is mostly associated with the thick separator. Therefore, OCP (green) is computed as the lithiation phase with the addition of half of this voltage difference. The curve is very close to the average between the two phases (yellow), apart from the extremes, where some hysteresis occurs. This test was conducted on 13 cells, showing little variabilities, as described in Section S3 of the

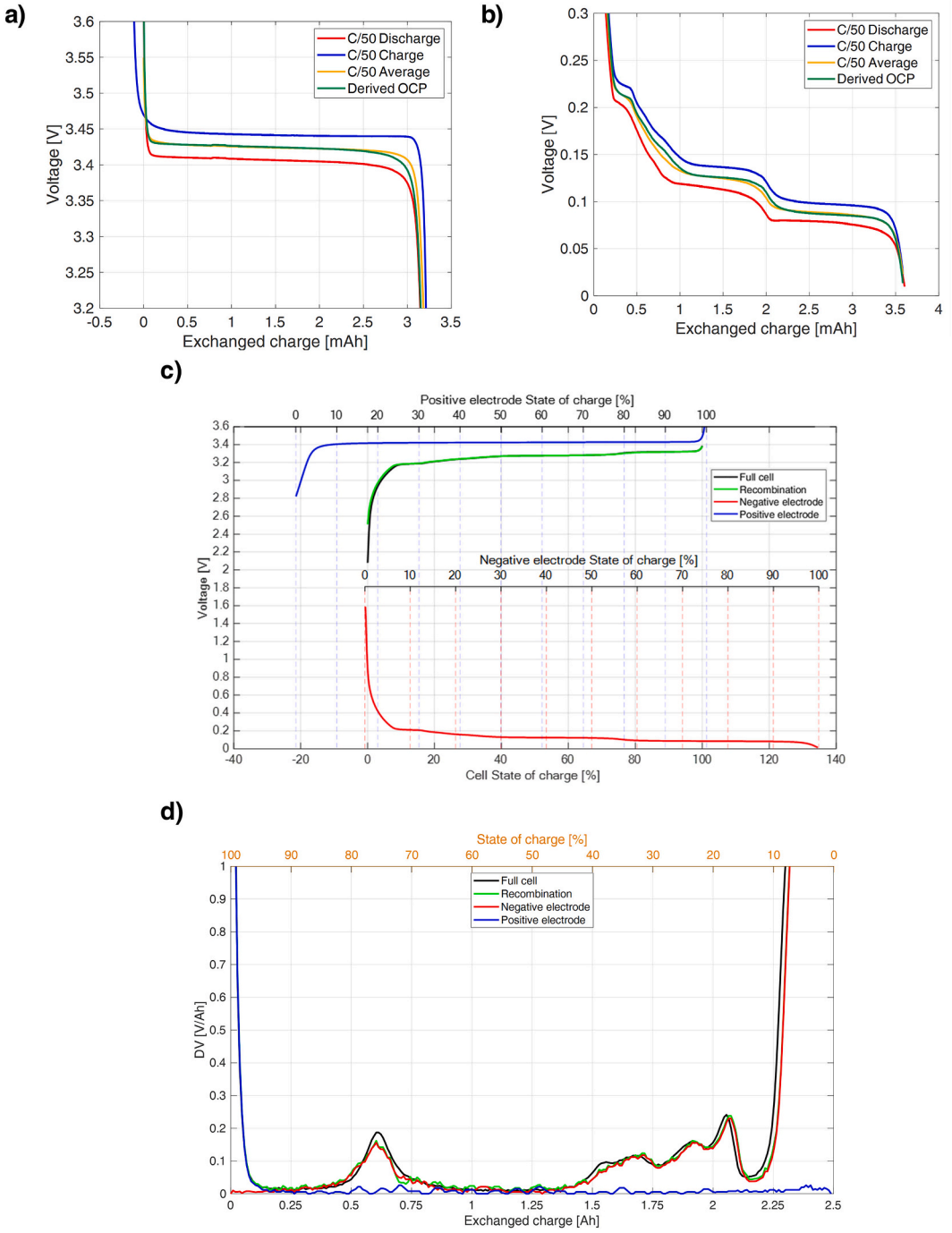

Fig. 3. Lithiation, delithiation, average and derived OCP of one cell for (a) LFP and (b) graphite materials. (c) Discharge curve with electrodes OCP matching. (d) Differential voltage with single electrode contributions. "Recombination" for the difference between positive and negative curves. DV contributions are taken as absolute values to ease the comparison.

Supplementary Materials.

Fig. 3b displays the same curves for the negative electrode half-cell. Graphite shows the usual three plateaus, as observed in the full cell discharge. Slight hysteresis is detected also here, especially at high voltage. No significant difference in capacity is recorded between the two phases, probably because of the low voltage of Graphite|Li half cells, which do not trigger significant self-discharges. The OCP of graphite is derived (green curve) as for LFP. The variability among graphite half-cells is discussed in Section S3 of the Supplementary Materials.

3.2.2. OCP matching

Electrodes OCP are matched to better reproduce the full cell discharge. The result is provided in Fig. 3c. From this activity, the lithiation degree of both materials at 100% and 0% SoC are estimated and fed to the models. These data are reported in Table 3, together with all the model parameters. Layers thickness and cross-sectional area are measured during the cell opening while the electrode solid volume fractions are fitted. The comparison between the experimental (black curve) and modelled (green) C/10 25 °C discharges is showed Fig. 3c–d in terms of discharge curve and differential voltage. The agreement is

Table 3
List of physical model parameters with estimation method and literature references. Estimation method: Lit. = obtained from literature, Meas. = experimentally measured, Ass. = assumption based, Fit. = model calibration on experimental measurement.

Parameter	Symbol	Negative electrode	Electrolyte/cell	Positive electrode	Estimation method	Ref.
Cross section [m^2]	A_c	–	0.1886	–	Meas	–
Layer thickness [μm]	L_i	45	25	70	Meas	–
Solid volume fraction [−]	$\varepsilon_{s,i}$	0.4775	–	0.378	Fit	[31,33–35]
Liquid volume fraction [−]	$\varepsilon_{l,i}$	0.33	0.54	0.332	Lit	[29–31,35]
Inactive material volume fraction [−]	$\varepsilon_{i,i}$	0.2225	0.46	0.29	Fit	–
Maximum lithium concentration [mol m^{-3}]	$c_{s,max,i}$	31,000	–	22,806	Lit	[29,31,35,36]
Stoichiometry at SoC 100% [−]	$x_{100\%}$	0.7446	–	0.0147	Fit	[36]
Stoichiometry at SoC 0% [−]	$x_{0\%}$	0.005	–	0.7246	Fit	[36]
Current collector resistance [mΩ]	R_{cic}	–	3.25	–	Fit	–
Kinetic rate constants [m s^{-1}]	k_0	1.82e−09	–	3.67e−11	Fit	[33,37]
Double layer specific capacitance [F m^{-2}]	C_{dl}	0.021	–	1.560	Fit	[38,39]
Solid-state lithium diffusivity constant [m^2 s^{-1}]	$D_{s,0}$	1.48e−15	–	1.22e-16	Fit	[40–43]
Electrolyte conductivity factor [−]	$cond_{el}$	–	0.2672	–	Fit	[40,44,45]
Activation energy for kinetic constant [J mol^{-1} K^{-1}]	EA_k	20,000	–	30,000	Lit	[33,37,38]
Activation energy for diffusion constant [J mol^{-1} K^{-1}]	EA_D	38,600	–	40,000	Lit	[33,37,38]
Particle radius [μm]	r_p	1.1	–	0.076	Lit	[29,31,35]
Electronic conductivity [S m^{-1}]	σ_s	100	–	0.5	Lit	[40,46,47]
Lithium transference number [−]	t_0^+	–	0.3753	–	Lit	[40,44,45]
Cathodic transfer coefficient [−]	α_c	0.5	–	0.5	Ass	–
Anodic transfer coefficient [−]	α_a	0.5	–	0.5	Ass	–
Reference temperature [°C]	T_0	25	–	25	Ass	–
Active material specific heat [J kg^{-1} K^{-1}]	C_{am}	–	1100	–	Lit	[36]
Active material density [kg m^{-3}]	ρ_{am}	–	2047	–	Lit	[36]
Active material radial thermal conductivity [W m^{-1} K^{-1}]	$k_{T,rad,am}$	–	52.35	–	Lit	[29–31,35]
Active material axial thermal conductivity [W m^{-1} K^{-1}]	$k_{T,ax,am}$	–	1.04	–	Lit	[48]
Chamber convective heat transfer coefficient [W m^{-2} K^{-1}]	h_{conv}	–	15	–	Ass	–
Mandrel radius [mm]	r_{mn}	–	2	–	Lit	[48]
Active material thickness [mm]	r_{am}	–	10	–	Lit	[48]
Steel case thickness [m]	r_{sc}	–	1	–	Lit	[48]
Cell radius [mm]	r_b	–	1.3	–	Meas	–
Cell height [mm]	H	–	6.5	–	Meas	–
Mandrel specific heat [J kg^{-1} K^{-1}]	C_{mn}	–	1700	–	Lit	[48]
Mandrel density [kg m^{-3}]	ρ_{mn}	–	1150	–	Lit	[48]
Mandrel radial thermal conductivity [W m^{-1} K^{-1}]	$k_{T,rad,mn}$	–	0.26	–	Lit	[48]
Mandrel axial thermal conductivity [W m^{-1} K^{-1}]	$k_{T,ax,mn}$	–	0.26	–	Lit	[48]
Steel case specific heat [J kg^{-1} K^{-1}]	C_{sc}	–	475	–	Lit	[48]
Steel case density [kg m^{-3}]	ρ_{sc}	–	7850	–	Lit	[48]
Case radial thermal conductivity [W m^{-1} K^{-1}]	$k_{T,rad,sc}$	–	44.5	–	Lit	[48]
Case axial thermal conductivity [W m^{-1} K^{-1}]	$k_{T,ax,sc}$	–	44.5	–	Lit	[48]

satisfactory.

3.3. Fresh cell - model

The parameters for a fresh cell are identified and the corresponding simulations of discharges and EIS at different operating conditions are reported in Fig. 4, while the parameters value is reported in.

Some discharges at C/10, 1C and 10C are shown at 10 °C, 25 °C and 40 °C in Fig. 4a, b, and c, respectively. The model (dark lines) reproduces the major trends with temperature and C-rate. The results are satisfactory even at 10C. One limitation arises at a low C-rate, where the 1C discharges show the staging behaviour of graphite clearly while they are

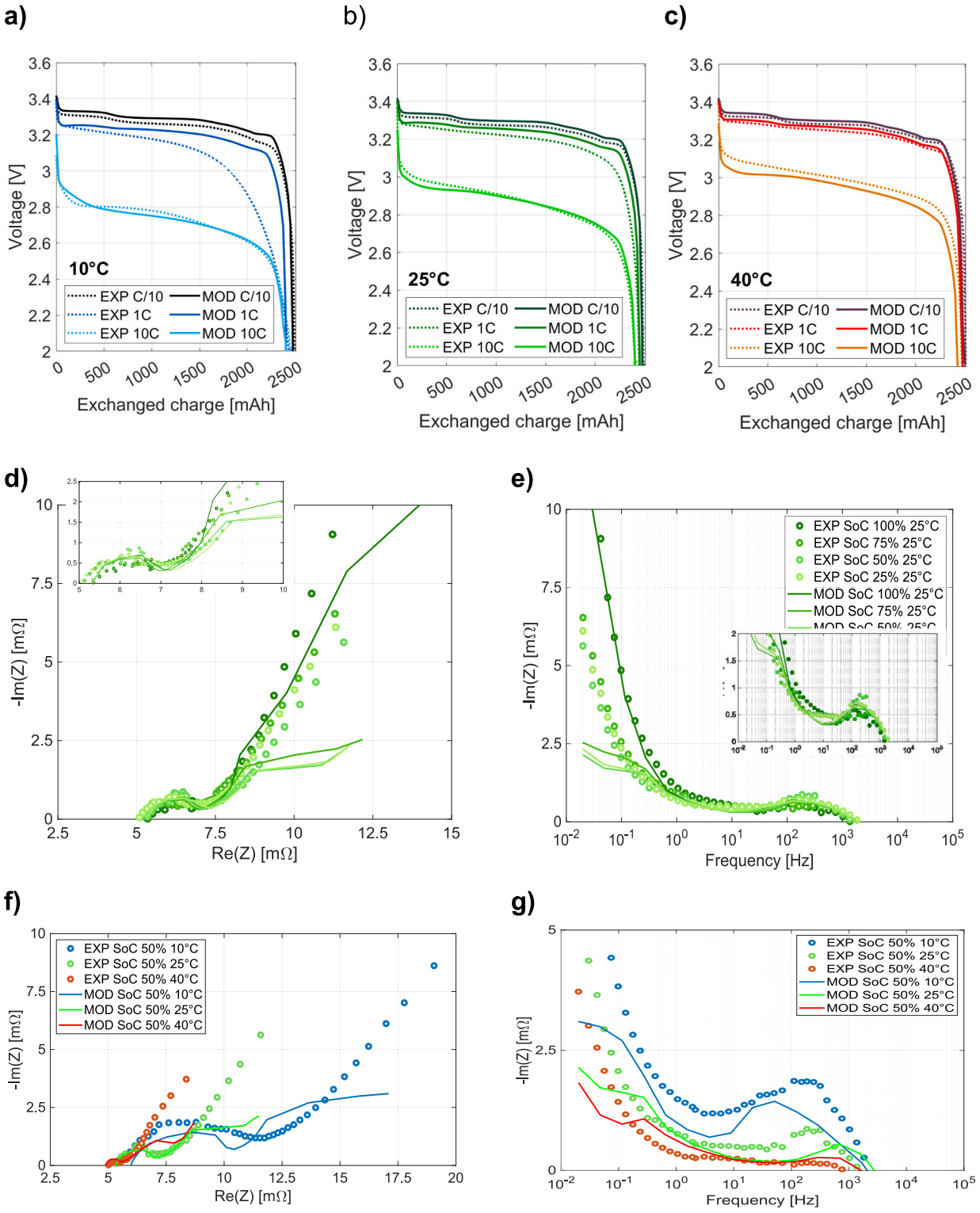

Fig. 4. Model simulations compared to experimental curves for a fresh cell of discharges at (a) 10 °C, (b) 25 °C and (c) 40 °C at different C-rates, (d) Nyquist plot of EIS and (e) Bode plot of imaginary component of the impedance at 25 °C and various SoC, (f) Nyquist plot of EIS and (g) Bode plot of imaginary component of the impedance at SoC 50% and various temperatures.

already blurred in the experimental curves. On the other hand, larger losses at this rate would imply too large losses at 10C. These results are in line with the best available in the scientific literature [29–33] on similar cells, considering the wide range of operating conditions.

EIS is investigated at varying SoC at 25 °C (Fig. 4d) and at varying temperatures at 50% SoC (Fig. 4f). The model captures the main phenomena and trends reasonably. Due to the small particle radius, the LFP impedance is almost negligible in the full cell spectrum. At 100% SoC, the model reproduces the diffusive branch properly, while it underestimates at all the other SoCs. The kinetic loop and high-frequency resistance are in line with the experiments, as depicted in the insets. The frequency of the peak is well reproduced, too. Regarding the temperature effect, the model slightly overestimates the HFR variation and the peak frequency reduction at decreasing temperatures while it slightly underestimates the variability of the loop size. At low frequencies, the same underestimation of the diffusive branch is evident. Again, the results are considered satisfactory.

3.4. Aged cells - testing

3.4.1. Residual capacity

Approaching the aged samples, residual capacity is selected as an indicator to provide an overview of the situation. The value of all the tested cells, measured through C/10 discharge, is reported in Table 4.

It is possible to notice that:

- The first string shows residual capacities lower than 10% for all the cells.
- There is a large spread of the results within the string, where the residual capacity is higher for cells located at the inlet section of the cooling stream (numbers 5 to 8). This result, though unexpected, agrees with the work of Katrina Ramirez-Meyers et al. [20] on the same cells and battery pack type.
- Strings with similar warning counts (e.g. A0802 vs A0602 and A0812 vs A0605) show similar residual capacities.
- Cells numbered 5-6-7-8 show similar values both for high and low warning counts.
- Cells manufactured in 2016 (type B) still exhibit very large values, over 95%.

These observations are now discussed in detail with an extensive set of measurements. Before that, the first string is regarded as a failed case, and it is neglected in the next analyses. Fig. S5 in the Supplementary Materials shows one damaged cell as an example.

3.4.2. EIS

The strong heterogeneity inside the strings was not expected. Thus, it is firstly verified with EIS. Table 5 reports the distribution of high-frequency resistance (HFR) and charge transfer resistance (RCT) for all the cells of strings A0802 and A0812, as an example. The full EIS spectra are available in FIG. S6 of the Supplementary Materials. The same heterogeneity is displayed in the impedance, with lower HFR associated with cells that exhibit higher residual capacities. Another big difference lies at intermediate frequencies, where the most aged cells show a bigger RCT with a lower characteristic frequency. Comparing strings A0802 and A0812, cells 7 and 8 show similar results, while cells 1 and 2 have different resistances, as already observed in the residual capacity analysis. Lastly, the impedance of strings with similar warning counts (e.g. A0802 vs A0602 and A0812 vs A0605) show similar trends in agreement with the capacity measurements. For clarity, plots of residual capacity, HFR and RCT as a function of cell position within each string have been added to the Supplementary Materials (Fig. S10), highlighting the consistent positional trend observed across all 2013 samples.

Both techniques identified a strong heterogeneity. Post-mortem analyses and model simulations are then applied to understand the degradation that these cells underwent. The analysis is then focused on these samples since cell B seems very close to a fresh state and this early consideration is verified with differential voltage analysis and EIS.

3.5. Aged cells – post-mortem analysis

3.5.1. Visual inspection

One very aged cell is opened in an inert environment with the procedure described in Section 2.7, namely cell A08122. Some pictures of the electrodes are reported in S7 of the Supplementary Materials. The roll is visibly wet thus, a large quantity of electrolyte is still present in the cell. LFP looks undamaged and glossy, like fresh. It only shows vertical pressure lines due to the usage in a cylindrical cell. Graphite is more brittle and not uniformly coloured. It is blue in the middle and brownish at the edges, with some white layers.

3.5.2. Half-cell Q-OCP

10 working LFP/Li cells and 16 Graphite/Li cells are built with harvested material, punched from different positions of the roll.

Fig. 5a reports the DV curve of charge and discharge phases of all the graphite half-cells, which shows how the test is strongly repeatable. The cell-to-cell variability of capacity is within 3.5% for both phases, with neither great differences due to self-discharge nor variations due to the position in the roll. An average decrease of capacity in the order of ~10% is measured, which is an indicator of LAM_{NE}. Also, a comparison of the DV of fresh and aged graphite against lithiation level is shown in

Table 4
Residual capacity in absolute and relative terms. Cells B are referred to as M1B nominal capacity.

String	A0811		A0802		A0602		A0812		A0605		B0101		B0112	
Cell	[mAh]	[%]	[mAh]	[%]	[mAh]	[%]	[mAh]	[%]	[mAh]	[%]	[mAh]	[%]	[mAh]	[%]
1	21	0.9	1584	68.9	1530	66.5	1272	55.3	1214	52.8	2428	97.1	2399	96.0
2	137	6.0	1589	69.1			1332	57.9						
3	157	6.8	1631	70.9	1640	71.3	1360	59.1	1360	59.1	2392	95.7	2392	95.7
4	144	6.3	1542	67.0			1284	55.8						
5	178	7.7	1807	78.6	1876	81.6	1537	66.8	1614	70.2	2430	97.2	2408	96.3
6	187	8.1	1772	77.0			1582	68.8						
7	212	9.2	1841	80.0	1882	81.8	1800	78.3	1778	77.3	2467	98.7	2457	98.3
8	138	6.0	1808	78.6			1730	75.2						
1	21	0.9	1584	68.9	1530	66.5	1272	55.3	1214	52.8	2428	97.1	2399	96.0
2	137	6.0	1589	69.1			1332	57.9						
3	157	6.8	1631	70.9	1640	71.3	1360	59.1	1360	59.1	2392	95.7	2392	95.7
4	144	6.3	1542	67.0			1284	55.8						
5	178	7.7	1807	78.6	1876	81.6	1537	66.8	1614	70.2	2430	97.2	2408	96.3
6	187	8.1	1772	77.0			1582	68.8						
7	212	9.2	1841	80.0	1882	81.8	1800	78.3	1778	77.3	2467	98.7	2457	98.3
8	138	6.0	1808	78.6			1730	75.2						

Table 5
High-frequency resistance (HFR) and charge transfer resistance (RCT) values from EIS at 50% SOC in [mΩ]. BoL reference values are HFR = 5.1 mΩ and RCT = 1.6 mΩ. More details on how these values have been measured are in Supplementary Materials S6.

String	A0802		A0602		A0812		A0605		B0101		B0112	
Cell	HFR	CTR	HFR	CTR	HFR	CTR	HFR	CTR	HFR	CTR	HFR	CTR
1	9.47	5.93	10.61	9.29	10.91	9.49	11.21	11.29	6.06	2.44	5.90	2.90
2	9.88	6.32			10.85	10.95						
3	10.04	5.76	10.42	8.18	10.31	10.99	11.54	10.26	5.51	2.49	5.42	2.58
4	9.75	6.65			10.50	12.30						
5	9.24	4.76	9.18	5.02	10.27	6.93	10.17	6.83	5.72	2.28	5.79	3.21
6	9.25	4.45			10.13	6.77						
7	8.44	3.96	8.62	5.28	8.95	4.65	9.06	5.44	5.55	2.45	5.21	2.99
8	8.73	3.47			9.52	5.48						

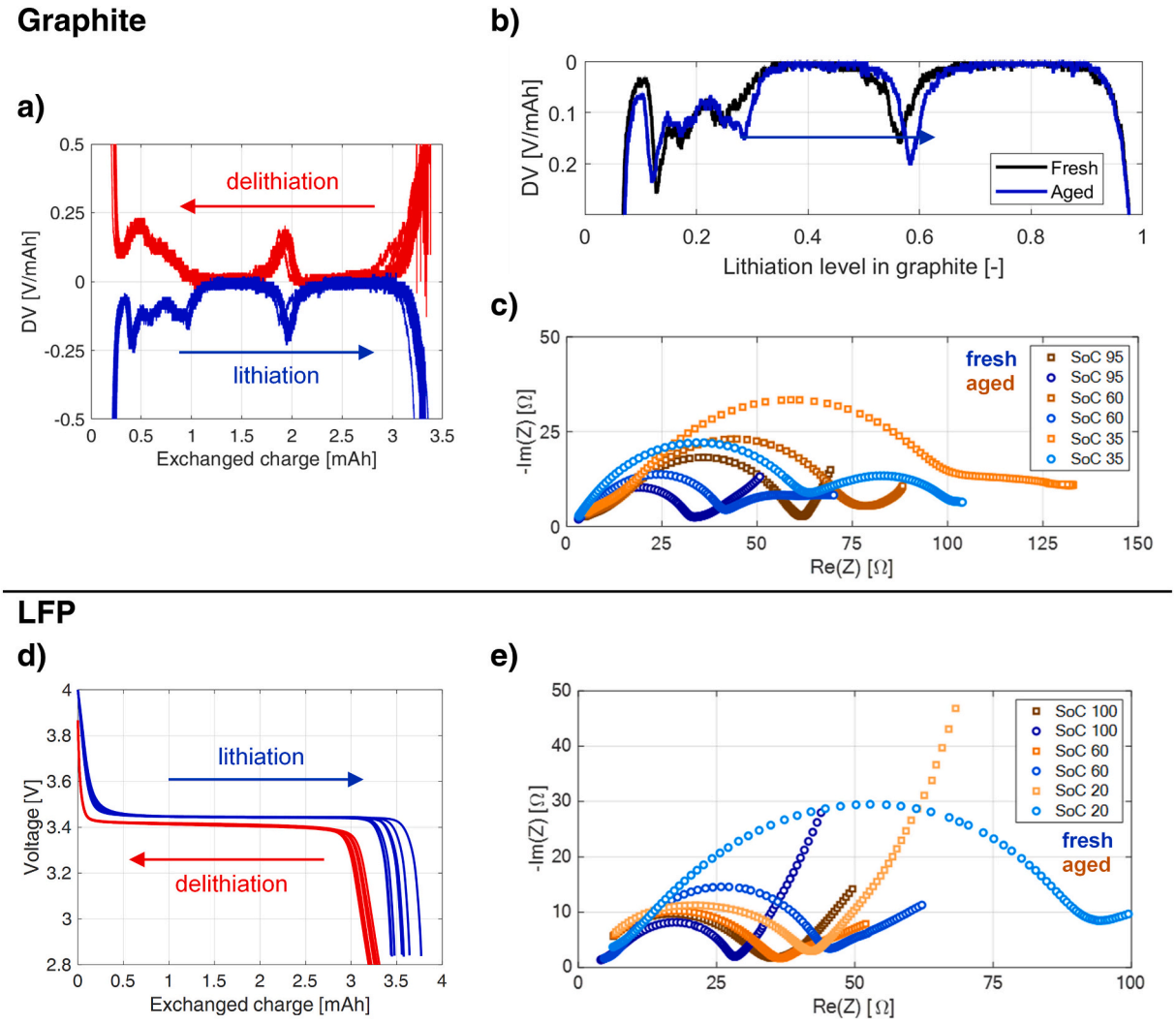

Fig. 5. GRAPHITE: (a) DV of C/50 de/lithiation cycles of 16 aged half-cells, together with (b) comparison of lithiation of fresh (blue) and aged (orange) electrodes. LFP: (d) OCP of C/50 de/lithiation cycles of 10 aged half-cells. (For interpretation of the references to colour in this figure legend, the reader is referred to the web version of this article.)

Fig. 5b. It corresponds to the comparison between M1B and M1A. Despite they are little, few differences arise, which can lead to misinterpretation of the degradation effects.

Fig. 5d shows the C/50 cycles of the LFP half-cells. The variability of capacity retention of LFP is less than 9% and 3.5% in the discharge and charge phases, respectively. The value of capacity retention is in line with that of the fresh material and no major variation of the OCP curve is detected. From these early observations, half-cell cycling confirms the small degree of degradation of the material, as in the visual inspection.

Comparison between EIS Nyquist plot at several SoCs of fresh and aged (e) LFP and (e) graphite half-cells. Blue shades for fresh materials, orange shades for aged ones.

3.5.3. *Half-cell EIS*

EIS of half-cells is performed, as specified in Section 2.7, on two aged cells for each type as well as on two fresh samples. Fig. 5c and e report the comparison of fresh and aged Nyquist plots for three SoCs, while the full description of EIS variations at varying SoCs is provided in FIG. S8 of

the Supplementary Materials.

LFP EIS shows a limited variability with SoC in the aged sample compared to the fresh one. In both cases, the kinetic loop increases with increasing SOC but with clearly different magnitudes (Fig. 5d). Overall, the different behaviour may be related to the improved cell design from M1A to M1B, and no major differences are evident as signs of degradation.

A good repeatability, both qualitatively and quantitatively, is observed for the graphite EIS of the two tested cells. As in the fresh case, it shows a linear tail at high frequency, followed by a kinetic loop and a diffusion branch. Comparing the spectra at corresponding SoCs (Fig. 5c), the aged cell shows a larger imaginary component of the impedance, around 1.5 times. Overall, the variations in the semicircle magnitude and frequency seem to be the most relevant differences. Though part of the differences might be related to the improved cell design M1A-M1B, a large share is likely to be associated with degradation, indicating a significant worsening of the reaction kinetics. Based on this analysis, the model calibration is performed.

3.5.4. Imaging and EDS

Laser microscopies and SEM are reported for fresh and aged electrodes in Fig. 6, enabling the comparison between different degradation states.

Concerning the fresh samples, LFP appears very homogeneous and flat in Fig. 6a. However, Fig. 6c reveals a flake-like structure in the micron-scale despite the expected nano-structure. The chemical

Table 6
Chemical composition by atomic mass of fresh and aged electrodes. Values are average. NB: S, V, Co, Ni, Zr and Hf are not reported being equal to 0.

Electrode	Element atomic fraction [%]						
	C	O	F	Al	P	Fe	Cu
Positive (fresh)	29.2	43.37	4.47	0.47	11.11	10.93	0
Negative (fresh)	90.94	5.74	2.97	0	0.14	0	0.2
Positive (aged)	31.1	42.7	7.53	0.1	9.6	9.01	0
Negative (aged)	47	42.3	8.66	0.1	1.5	0.17	0.3

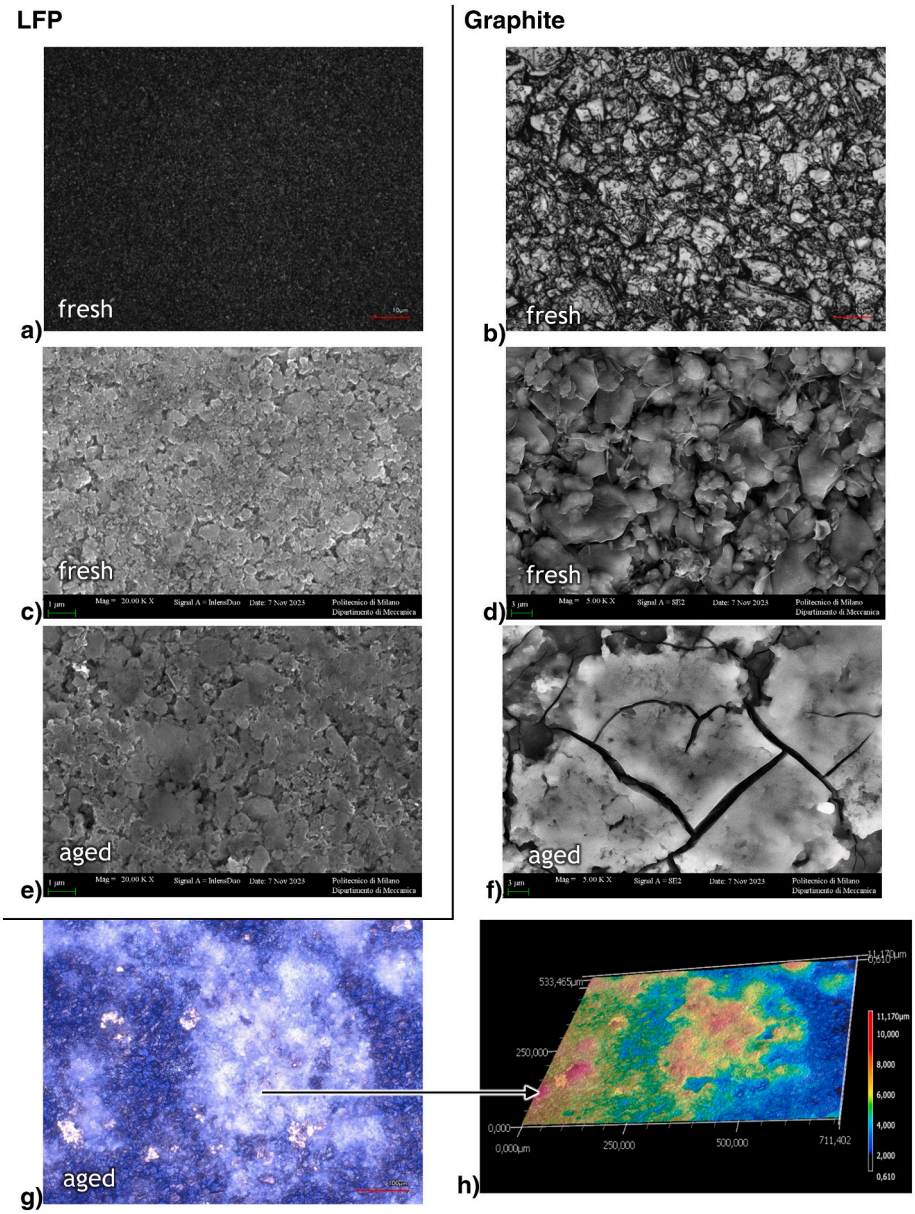

Fig. 6. Microscopies of a fresh and aged electrodes. Laser microscopies of (a) fresh LFP and (b) fresh graphite at 150×. SEM images of (c) fresh LFP at 20,000×, (d) fresh graphite at 5000×, (e) aged LFP at 20,000× and (g) aged graphite at 5000×. Optical microscopy of aged graphite at 20× magnification with (h) height analysis.

composition (Table 6, first line) is consistent with the LFP chemistry, with additional conductive carbon to improve the low electronic conductivity of the material. The microscopy of graphite in Fig. 6b reveals a flake structure consistent with the power-oriented design of the cell. On top, some filaments are present, which may be conductive elements to further improve the performance. From Fig. 6d, the size of the flakes is estimated to be around 8 μm. The composition is carbon-based, with some oxygen, fluorine and phosphorus, which can be associated with the binder, the initial SEI and salt precipitates from electrolyte.

Regarding aged sample, optical and laser microscopies of the aged LFP are omitted due to the limited amount of information. The SEM image (Fig. 6e) shows a uniform and flat surface, with flake-type microstructures which resemble the figures of the fresh material (Fig. 6c). Regarding the chemical composition (Table 6), it is similar to the outline of the fresh cell. However, it is impossible to assign these slight differences to degradation rather than a different cell design. These final measurements further support the limited degradation level of this material. On the other hand, optical microscopy of the surface of the negative electrode shows the deposition of white components on top (Fig. 6f). Laser-microscopy height analysis (Fig. 6g) confirms that these surface deposits form a continuous passivation layer located above the graphite particles, reaching thickness values up to ~11 μm in the most affected regions. The underlying, uncovered areas maintain a morphology similar to the fresh electrode, with flake-like graphite particles of comparable size and preserved conductive filaments. The particles are covered with a uniform semi-transparent layer, also showing many cracks. EDS (Table 6) revealed that the carbon share is half of the value of the fresh cell, while oxygen and fluorine are much larger. Both the visual appearance and the chemical composition suggest that this layer is constituted by SEI and general residues from electrolyte decomposition and salt precipitation. Still considering limited quantitative reliability of EDS measurements, low iron content is estimated, indicating no crossover consistently with the relatively low temperature of operation. It is worth to stress that, in subsequent activities, analogous analyses have been performed on harvested materials from other single-cell samples with miscellaneous ageing of the same population, hereby not reported because out of the scope, and identified to have a lower development of such layer, which then consistently appears as related to battery ageing state.

3.6. Aged cells – model

3.6.1. DVA

Differential voltage analysis is performed. The equilibrium model is applied to estimate quasi-equilibrium capacity losses. The lumped resistance is equal to 22 mΩ and 30 mΩ for fresh and aged cells, respectively. Moreover, consistently with LFP being known as very stable against degradation [13], its LAM is firstly assumed to be negligible with respect to other contributions. Then, such assumption is later verified with cycling of harvested LFP material in half-cell configuration (Section 3.5).

It is worth to stress the impact of OCP curves on such simulations. They were initially derived from the literature, from which a wide variability in the graphite curves appeared, that affected the reliability of the simulations, significantly affecting the results of the analysis. A second attempt was performed with the OCP curves of a fresh M1B cell, but this solution showed non-negligible differences between the OCP curve of M1A and M1B graphite, as reported before by comparing the DV of graphite half-cells. Therefore, the analysis is performed by exploiting the OCP curve of the aged cell. This choice is supported by the simulations of C/50 discharges, where the characteristic peaks and valleys of the DV plot are further magnified. Some cases are depicted in Fig. 7a,b,c. Three cells with different degradation extents are provided, together with the model simulations. The shape of the graphite curve is the same and resembles the shape of the M1A graphite curve, disregarding the degradation level. Hence, to further minimise the impact of M1A–M1B design differences on the ageing analysis, the q-OCP fitting is performed using the experimentally measured graphite OCP from an M1A cell, so that the identification of LLI and LAM_{NE} relies on the exact chemistry representative of the aged samples.

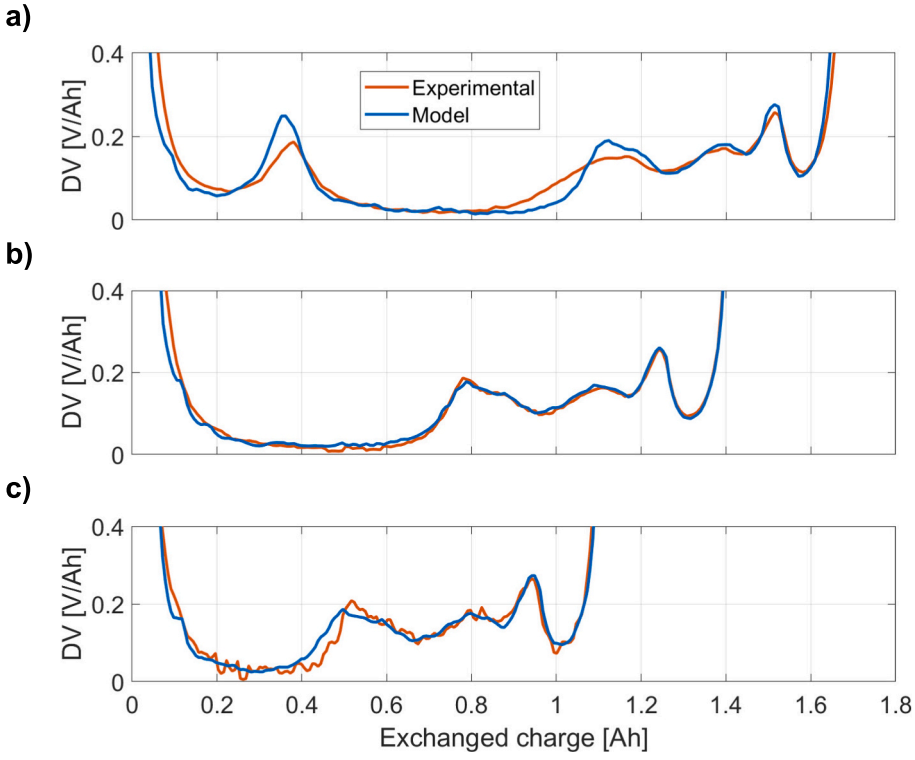

Fig. 7. Experimental (orange curve) and modelled (blue) differential voltage curves of cells (a) A06205, (b) A08126 and (c) A08124 at C/50 25 °C. (For interpretation of the references to colour in this figure legend, the reader is referred to the web version of this article.)

3.6.2. Quasi-equilibrium ageing parameters evolution

Model simulations, executed as described in Section 2.6, are in very good agreement with the experiments. The values of LLI and LAM_{NE} for these simulations are reported in Table 7. As expected, LLI grows with lower residual capacity, since LAM_{NE} is considered purely delithiated, so LLI is the only source of lithium loss. It is worth to stress that, following such assumption, losses cannot be expected in summing up resulting in lost capacity value, because a possible share of lithiated LAM_{NE} would also contribute to LLI. It is confirmed by the shape of the DV curve, where the first peak, corresponding to the transition between the first and second graphite plateaus, is missing in Fig. 7b–c, therefore, graphite is poorly lithiated at cell SoC 100%. The disappearance of the graphite stage I–II transition peak in highly aged cells indicates that the negative electrode no longer reaches the high-lithiation compositions required for this transition. This behaviour is reproduced by the q-OCP model through LLI variations only and is consistent with the sensitivity analysis on identifiability characteristics performed over quasi-equilibrium DV analysis discussed in [26], where LLI remains well identifiable while the identifiability of LAM_{NE} decreases as graphite staging features fade. In this perspective, the absence of a clear trend in the estimated LAM_{NE} values is coherent with its inherently limited identifiability under such extremely aged conditions.

3.6.3. Focus on LAM_{NE}

To deepen the understanding of this feature, a dedicated sensitivity analysis is provided in Fig. 8 to highlight the effect of LAM_{NE} on two differently-aged cells. "Model best fit" (black curve in Fig. 8a–d) is the solution provided by the algorithm, which minimises the cost function. Two further simulations are added: in the green case, LLI and LAM_{NE} obtained by the algorithm are raised by 1% and 6%, respectively. In the blue case, both terms are decreased by the same amount. LLI is varied to match the last valley of the DV to ease the comparison among the curves.

In Fig. 8a–b, this analysis is performed on a little-aged cell. In this case, it is possible to visualise that there is a clear best-fit case. Indeed, in both the green and the blue cases, it is easy to identify an over/under-estimation of LAM_{NE}, respectively, because the peak at 0.4 Ah is sensitive to LAM_{NE}, with a very good fit only for the "Model best fit" case.

Differently, Fig. 8c shows the same sensitivity analysis performed on a severely aged sample. It appears that the green case underestimates the residual capacity, thus introducing more losses than their proper magnitude. However, the DV results (Fig. 8d) are close to the experiments, both in magnitude and in position of the main characteristics. On the contrary, the blue curve better approximates the residual capacity, providing slightly worse results on the DV around 0.5 Ah. Between green and blue cases, LLI varies within 2%; thus, its value is very stable. Differently, LAM_{NE} varies by 12%, raising some questions on the reliability of the estimation. The lack of the phase transition peak at high SOC in the DV curve clearly results in a loss of identifiability of LAM_{NE}.

As a result of the analysis, the simulation of the less-aged cell looks more reliable, while for very-aged cells, further verifications are performed.

3.6.4. Charge-based estimation of LAM_{NE}

To overcome these limitations, a charge-based method is developed. As a common practice in literature [11], LAM_{NE} of LFP|Graphite cells can be estimated by comparing the distance between two relevant peaks of the graphite OCP. The usual approach involves the distance between the high SoC peak, that is, the transition between the first and second plateau, and the peak corresponding to the transition between the second and third plateau [17]. Here, the method is extended, looking for a different feature to be compared between fresh and aged cells in order to be applied to all the tested cells. In particular, 4 couples of relevant points are proposed. With reference to Fig. 8e,

- Point A: the position where DV achieves 0.1 V/Ah
- Point B: the flattening due to the 2 L to 3 L transition of graphite [49]
- Point C: the largest peak of the DV
- Point D: the minimum, last flat voltage plateau before the end of discharge
- Point E: end of discharge.

The difference in exchanged charge between these points is exploited as an indicator of LAM_{NE} for all the 2013 samples. The results collected over C/10 discharges are shown in Fig. 8f, together with the estimation of the usual method, labelled "Voltage-based". It is evident how all the methods provide quite different results. The green method exploits a small charge difference. It is possible to assume that it is the least reliable since measurement uncertainty and repeatability might affect the results in a non-negligible way. Other than this, all charge-based methods agree to identify more than 15% of LAM_{NE}. Yellow and red approaches are similar and seldom agree with the voltage-based method. The blue method estimates more than 20% LAM_{NE}. In summary, different charge-based methods are applied, but it is not possible to identify a proper value of LAM_{NE}. Most of the methods agree in 15% or more LAM_{NE}, similar to the reliable results collected with the voltage-based method on little-aged cells at C/50 discharge. Moreover, all methods show a little dependency on the residual capacity. Therefore, it is reasonable to assume LAM_{NE} in the order of 20%. LLI remains the dominant effect.

3.6.5. Kinetics and mass transport

The model is applied to simulate the 1C 25 °C discharge and 100% SoC 25 °C EIS after the identification of the quasi-equilibrium conditions. Differently from the main case study, in this case, the choice of the free parameters is derived from the results of the post-mortem analysis to compensate for the absence of a reliable BoL sample of the same type, simplifying the analysis. Therefore, the following decisions are made:

- **HFR**: the difference between fresh and aged HFR is taken into account in two ways:
  - o The current collector term is raised by 2 mΩ with respect to the BoL calibration, considering the different impedance at 1 kHz stated in the respective datasheets of model M1A and M1B.
  - o The remaining differences can be associated with a limited degradation of the electrolyte, either due to the electrolyte itself or to the growth of the SEI. Therefore, electrolyte conductivity and diffusivity are fitting parameters.
- **Kinetics**: there is a growing kinetic loop on aged cells. The more degraded the cell, the bigger the loop. According to the graphite half-cell, a worsening of the reaction is likely to have occurred. Thus, the negative electrode kinetic rate constant is considered as a fitting parameter.
- **Diffusion properties**: according to the BoL parameters, it is hard to define the properties such that both C/10, 1C and 10C discharges are properly reproduced. In the absence of evidence of degradation of these properties, they are assumed to be constant because their value cannot be identified reliably.

The values of the parameters are provided in Table 8 as a multiplication factor related to the BoL value, while the curves are provided in Fig. 9 for the cells belonging to string A0812 as an example. The peak frequency is similar among the cells, and the double-layer capacitance does not show major differences. Between the least and the most degraded cells, the kinetic rate constant can vary with a factor ~3,

Table 7
Quasi-equilibrium ageing parameters estimated for three cells at C/50 25 °C discharge.

Cell	Residual capacity	LLI	LAM_{NE}
A06025	81.6%	20.9%	19.7%
A08126	68.8%	32.0%	9.1%
A08124	55.8%	45.3%	11.0%

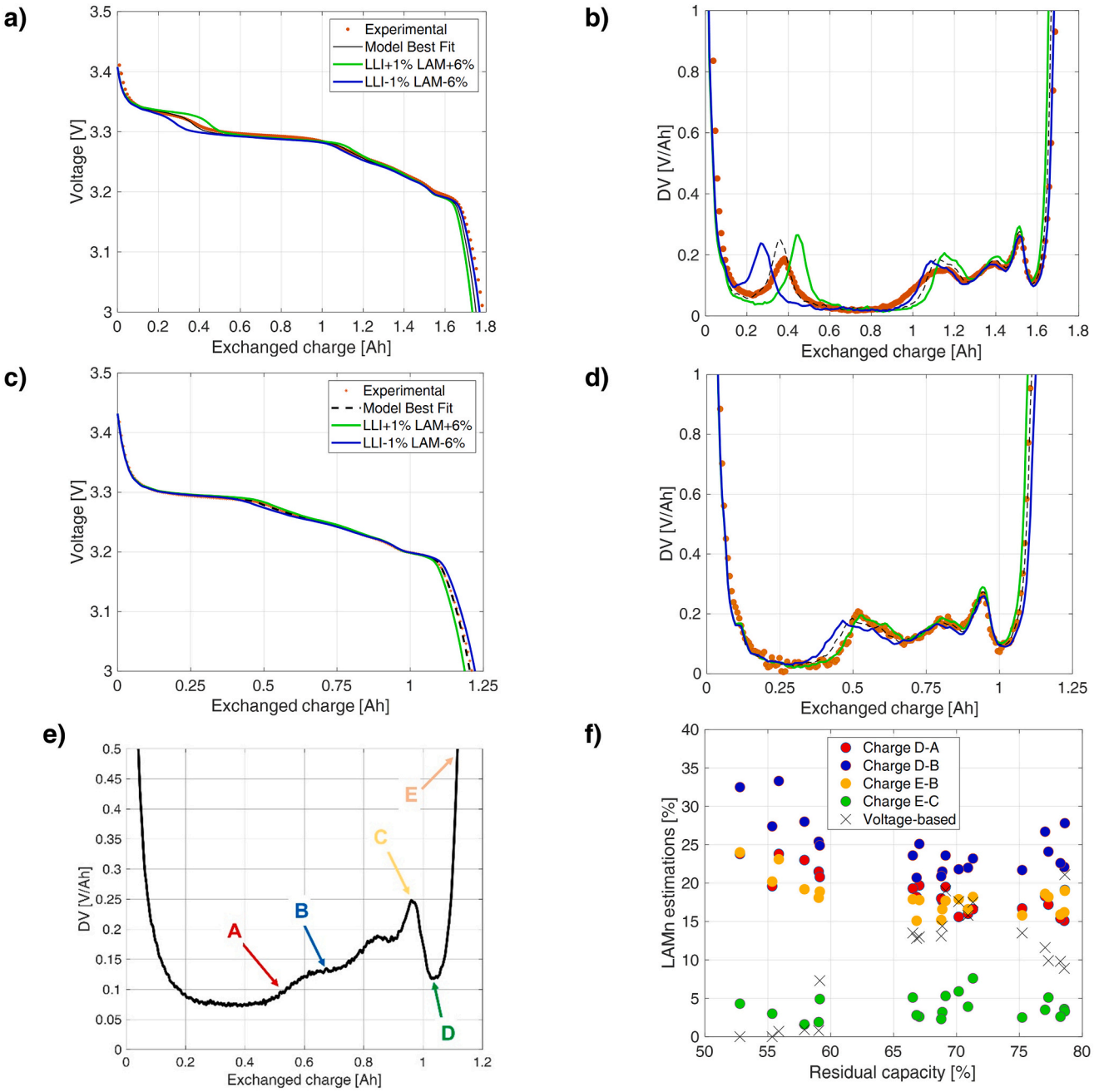

Fig. 8. Deepening on the sensitivity of the quasi-equilibrium analysis on the value of LAM_{NE}. (a) Discharge curve and (b) DV of cell A06025. (c) Discharge curve and (d) DV of cell A08124. Colour coding in the legend of subfigures (a) and (c). (e) Selection of the relevant points for the charge-based LAM_{NE} estimation. (f) Results with all the methods for all the C/10 discharges of 2013 samples.

Table 8
Parameters value for string A0812.

Cell	Residual capacity [%]	Electrolyte conductivity factor [−]	Kinetic rate factor [−]	Double layer capacitance factor [−]
A08121	55.3	0.5	0.17	0.40
A08122	57.9	0.5	0.17	0.40
A08123	59.1	0.7	0.12	0.35
A08124	55.8	0.5	0.12	0.40
A08125	66.8	0.6	0.23	0.37
A08126	68.8	0.7	0.21	0.37
A08127	78.3	1.0	0.30	0.30
A08128	75.2	0.8	0.28	0.30

reflecting the different sizes of the kinetic loop. Lastly, the HFR varies significantly, inducing a significant reduction of the electrolyte conductivity, up to 50% for the most aged cells. Overall, there is a good agreement with aged cells exploiting only three fitting parameters.

Discharges at 1C and different temperatures are reported in Fig. 9e–g. Only the electrolyte diffusivity is reduced by 50% to account for larger losses. It is in line with the electrolyte conductivity reduction. At 40 °C, the model simulations are quite in line with the experiments. Moving towards lower temperatures, higher losses arise, which are underestimated by the model, as for the fresh case, in order to enable 10C discharges. Differently from the fresh case, capacity varies sensibly with temperature. The model follows this trend with a slight underestimation. Overall, the results are considered satisfactory.

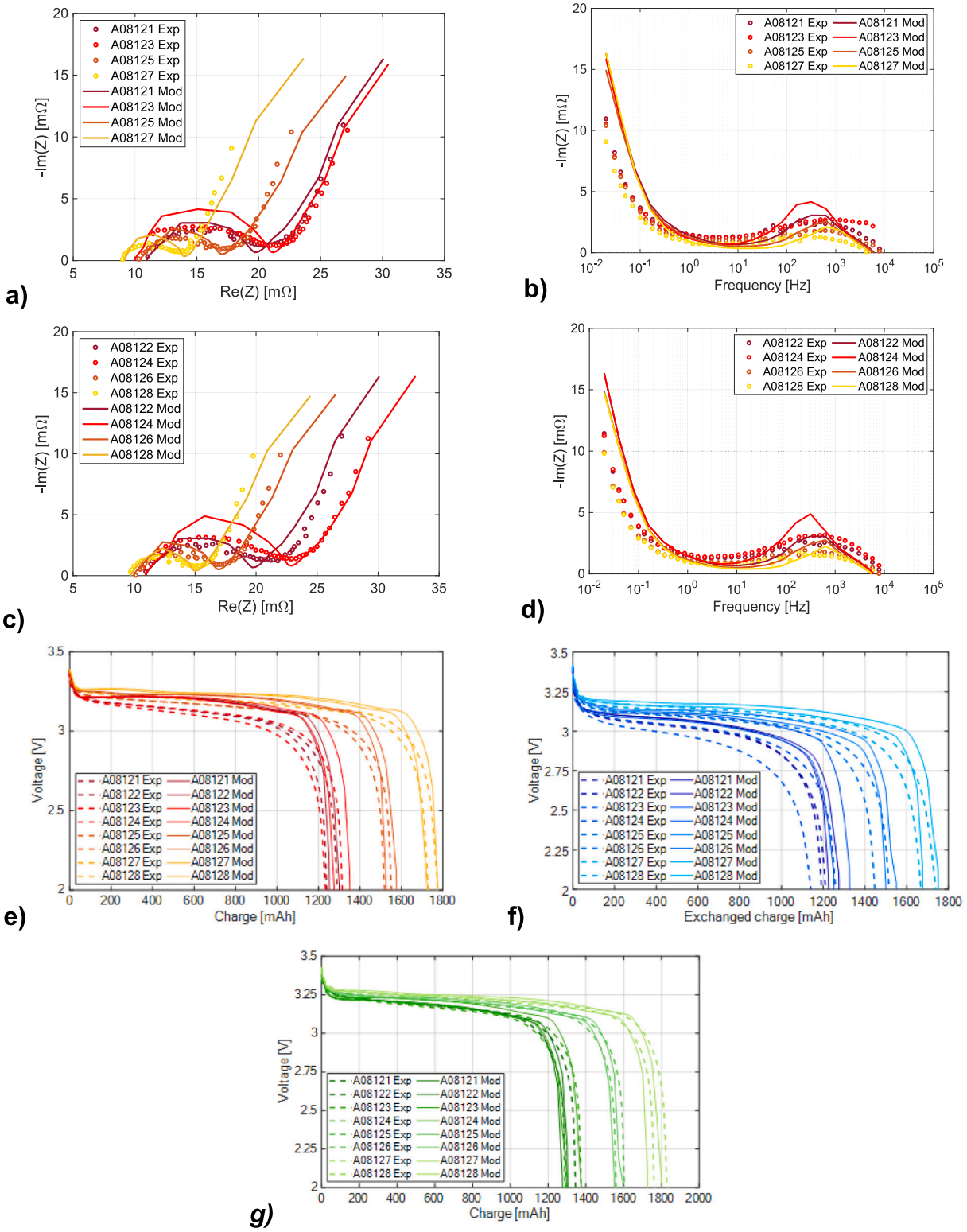

Fig. 9. Experimental and simulated EIS and discharge for cells of string A0812. (a) Nyquist and (b) Bode of the imaginary component of cells 1-3-5-7, (c) Nyquist and (d) Bode of the imaginary component of cells 2-4-6-8. (e) 25 °C, (f) 10 °C and (g) 40 °C 1C discharge of cells of the whole string A0812.

3.7. Aged cells – origin and interpretation of degradation

The analysis identified the following main observations

- Residual performances are largely heterogeneous, also within the same string, both in terms of capacity and impedance.
- DVA highlighted a significant lithium inventory loss as the dominant degradation mechanism. With different attempts, the most reasonable value of LAM_{NE} is estimated in the order of 20%. There is no evidence of a distribution of LAM_{NE} between cells of the same string, while LLI is strongly heterogeneous.

- The positive electrode does not show signs of degradation either in a visual inspection, microscopies at various scales, chemical composition and capacity retention with respect to the fresh cell.
- Graphite EIS shows an increase of magnitude by 50% at all SoCs and a shift to the lower frequency of its charge-transfer reaction.
- Graphite microstructure does not seem to vary due to ageing, but microscopies clearly illustrate its covering by a thick white layer, likely originated from electrolyte passivation and decomposition.
- The model is applied to reproduce the behaviour of aged cells in 1C 25 °C discharge and 100% SoC 25 °C impedance, explaining the major trends of losses exploiting the kinetic properties of the negative electrode and the conductivity of the electrolyte.

All the results lead to the conclusion that the LFP electrode is unaffected by ageing and that the most important degradation mechanism is related to SEI growth. This mechanism is in agreement with the reduction of electrolyte conductivity and loss of lithium and is suggested by SEM images and chemical composition. The dominant role of SEI and electrolyte degradation is further supported by the quantitative separation of LLI and LAM_{NE} obtained from q-OCP modelling and by the substantial reduction in electrolyte conductivity captured by P2D simulations. Consistently, post-mortem SEM/EDS reveals a thick surface layer on graphite, whereas the LFP electrode remains structurally robust. Together, these findings corroborate that ageing pathways predominantly affect the negative electrode and the electrolyte, rather than the LFP active material.

Considering the available information regarding the operation of the batteries on the vehicle, the origin of the heterogeneous behaviour is identified as a temperature effect. Indeed, the cells are assumed to be very similar in performance at a fresh state, as observed for the fresh cells tested in this campaign. They operate in parallel configuration, and no unbalancing is expected due to the external connections. The only anisotropy in the system is induced by the heating/cooling system. 5–10 °C average temperature difference, continued over 8 years, is likely to induce such a difference. A persistent inlet–outlet temperature difference of this magnitude can plausibly lead to ageing-rate accelerations of approximately 1.3–2× for a 5 °C increase and 2–4× for a 10 °C increase, fully in line with typical Arrhenius-type behaviour and consistent with the positional trends observed in residual capacity, HFR and RCT (see Fig. S10). This gradient of performance was evident in all the tested strings, including samples manufactured in 2016, though to a small extent. Moreover, internal temperature differences might have been even larger. Consistently, the directional pattern of ageing observed in all strings mirrors the long-term inlet–outlet temperature difference measured by the BMS; this trend is also clearly visible in the positional plots included in the Supplementary Materials—where residual capacity, HFR and RCT progressively improve from outlet-facing to inlet-facing cell positions—and is fully consistent with the spatial SoH distribution reported in [20], supporting uneven cooling as a plausible contributor to the observed heterogeneity.

Furthermore, this mechanism can feed on itself. Warm cells have a low resistance. In a parallel connection, the voltage of all the cells has to be the same. Thus, larger C-rates are expected for less resistive cells. Larger C-rates are likely to induce larger degradation, thus higher capacity loss and resistance increase, which, in turn, enhance the self-heating of the cell and, finally, its temperature. Lastly, a temperature gradient is consistent with a larger SEI growth since side-reactions kinetics is promoted at higher temperatures.

4. Conclusions

This work reports the state of health analysis of a batch of 24 end-of-life cells from a hybrid bus application, addressing the notable gap in extensive investigations of real-world samples in the literature. Fresh cells served as a performance benchmark and enabled the parameterization of a physical P2D model. These cells demonstrated very high rate capabilities and low impedance, suitable for high-power applications. The P2D model effectively replicated the discharge profiles and impedance of the fresh cells. However, applying these results to aged cells was limited by differences in cell releases, internal geometries, and graphite OCP. The characterisation of aged cells revealed significant heterogeneity in residual capacity (ranging from 80% to 55% of the BoL capacity) and impedance. This variability is crucial for managing second-life batteries and is likely related to the cells' positions within strings, influenced by uneven cooling effectiveness, as corroborated by thermal measurements from the BMS. To investigate the origins of degradation and heterogeneity, this study combined cell testing data, post-mortem analyses of a very aged sample, and physical modelling. The main findings include:

- **Loss of Lithium Inventory:** The q-OCV model indicated that LLI is the primary degradation mode. Estimating the loss of active material on the negative electrode (LAM_{NE}) was challenging due to the disappearance of graphite stage I-II transition peaks in the DV analysis of very aged cells. Alternative strategies validated against half-cell capacity measurements showed no more than 20% LAM_{NE}, confirming LLI as the dominant effect.
- **P2D Model Application**: The model was applied to aged cells to replicate behaviour during 1C 25 °C discharge and 100% SoC 25 °C impedance tests. It explained major loss trends by considering the kinetic properties of the negative electrode and the conductivity of the electrolyte.
- **Graphite Material Analysis**: SEM and EDS revealed a thick surface layer with significant oxygen and fluorine content, indicative of a electrolyte-decomposition products related layer. This finding aligns with the large LLI suggested by DV analysis and the decreased electrolyte conductivity, which accounts for increased overpotentials during discharge and the higher HFR in EIS.
- **LFP Material Robustness**: Various measurements confirmed that LFP material exhibited superior robustness against degradation.

In conclusion, decomposition and passivation of electrolyte, together with SEI growth, emerged as the dominant degradation mechanism, driven by charge-discharge cycles during bus operation and parking phases at warm temperature, leading to LLI. The heterogeneity is attributed to the thermal gradients experienced by each string due to anisotropic cooling with ambient air. Prolonged temperature differences likely led to varying SEI growth rates and residual performance discrepancies.

These findings also suggest practical implications for second-life applications. Given the strong intra-module heterogeneity observed, any meaningful screening must be performed at cell level, since pack-level data and the parallel electrical configuration do not allow the ageing contribution of individual cells to be resolved. Once modules are disassembled, simple impedance-based triage at cell level (e.g., HFR and RCT at 50% SoC), combined with disassembly strategies that account for cell position, may help mitigate variability. Furthermore, the substantial loss of extractable capacity limits reuse in energy-oriented applications, whereas the comparatively preserved impedance and high-rate behaviour indicate that repurposing in power-intensive second-life applications may remain viable.

Overall, this study provides an integrated and quantitative assessment of long-term, real-world LFP ageing, combining complementary electrochemical, modelling and post-mortem evidence, highlighting the practical challenges of performance heterogeneity within battery modules.

List of acronyms

Acronym	Description
BOL	Begin of life

(continued on next page)

(*continued*)

CTR	Charge Transfer Resistance
DV	Differential Voltage
EDS	Energy Dispersive X-ray Spectroscopy
EIS	Electrochemical Impedance Spectroscopy
HFR	High-Frequency Resistance
LAM	Loss of Active electrode Material
LLI	Loss of Lithium Inventory
LFP	Lithium-iron-phosphate battery
OCP	Open-Circuit Potential
P2D	Pseudo-two dimensional
PSO	Particle Swarm Optimisation
SEI	Solid electrolyte interphase
SEM	Scanning Electron Microscope
SoC	State of charge
XPS	X-ray photoelectron spectroscopy

CRediT authorship contribution statement

G. Sordi: Writing – review & editing, Writing – original draft, Visualization, Validation, Methodology, Investigation, Formal analysis, Data curation, Conceptualization. **G.M. Trippetta:** Writing – review & editing, Writing – original draft, Visualization, Investigation, Formal analysis, Conceptualization. **D. Luder:** Writing – review & editing, Methodology, Investigation. **S. Berg:** Methodology, Investigation. **W. Li:** Writing – review & editing, Supervision. **E. Figgemeier:** Supervision. **D. U. Sauer:** Supervision. **A. Casalegno:** Writing – review & editing, Supervision, Project administration, Funding acquisition. **C. Rabissi:** Writing – review & editing, Supervision, Project administration, Funding acquisition, Conceptualization.

Declaration of competing interest

The authors declare that they have no known competing financial interests or personal relationships that could have appeared to influence the work reported in this paper.

Acknowledgements

The authors would like to acknowledge IVECO Bus SpA for supporting this research, providing the samples and BMS data and pursuing scientific dissemination by sharing the results of the activity in this publication. The work is also partially supported by the European Union's Horizon Europe program [Grant Agreement No. 101138532, project "AutoMat - Compliant and fully AUToMATed circular solutions for multiple battery and battery embedded device enhanced by digital solutions"]. The authors would like to acknowledge also Ludovica Rovatti and Rasheed Michael Ishola for their help in performing SEM analysis. Moreover, G.S. would like to acknowledge the IDEA League for funding his research exchange at CARL, RWTH Aachen University, Germany.

Appendix A. Supplementary data

Supplementary data to this article can be found online at https://doi.org/10.1016/j.est.2026.120653.

Data availability

The dataset of the results described in this work is reported on Zenodo.

References

[1] D. Stampatori, P.P. Raimondi, M. Noussan, Li-ion batteries: a review of a key technology for transport decarbonization, Energies (Basel) 13 (2020), https://doi.org/10.3390/en13102638.
[2] G. Zubi, R. Dufo-López, M. Carvalho, G. Pasaoglu, The lithium-ion battery: state of the art and future perspectives, Renew. Sustain. Energy Rev. 89 (2018) 292–308, https://doi.org/10.1016/j.rser.2018.03.002.
[3] N. Nitta, F. Wu, J.T. Lee, G. Yushin, Li-ion battery materials: present and future, Mater. Today 18 (2015) 252–264, https://doi.org/10.1016/j.mattod.2014.10.040.
[4] J. Jyoti, B.P. Singh, S.K. Tripathi, Recent advancements in development of different cathode materials for rechargeable lithium ion batteries, J. Energy Storage 43 (2021), https://doi.org/10.1016/j.est.2021.103112.
[5] M. Kotal, S. Jakhar, S. Roy, H.K. Sharma, Cathode materials for rechargeable lithium batteries: recent progress and future prospects, J. Energy Storage 47 (2022), https://doi.org/10.1016/j.est.2021.103534.
[6] A. Barré, B. Deguilhem, S. Grolleau, M. Gérard, F. Suard, D. Riu, A review on lithium-ion battery ageing mechanisms and estimations for automotive applications, J. Power Sources 241 (2013) 680–689, https://doi.org/10.1016/j.jpowsour.2013.05.040.
[7] C.R. Birkl, M.R. Roberts, E. McTurk, P.G. Bruce, D.A. Howey, Degradation diagnostics for lithium ion cells, J. Power Sources 341 (2017) 373–386, https://doi.org/10.1016/j.jpowsour.2016.12.011.
[8] M. Zhang, Y. Liu, D. Li, X. Cui, L. Wang, L. Li, K. Wang, Electrochemical impedance spectroscopy: a new chapter in the fast and accurate estimation of the state of health for lithium-ion batteries, Energies (Basel) 16 (2023), https://doi.org/10.3390/en16041599.
[9] D. Li, D. Yang, L. Li, L. Wang, K. Wang, Electrochemical impedance spectroscopy based on the state of health estimation for lithium-ion batteries, Energies (Basel) 15 (2022), https://doi.org/10.3390/en15186665.
[10] D. Li, D.L. Danilov, J. Xie, L. Raijmakers, L. Gao, Y. Yang, P.H.L. Notten, Degradation mechanisms of C6/LiFePO4 batteries: experimental analyses of calendar aging, Electrochim. Acta 190 (2016) 1124–1133, https://doi.org/10.1016/j.electacta.2015.12.161.
[11] D. Li, D. Danilov, L. Gao, Y. Yang, P.H.L. Notten, Degradation mechanisms of C6/LiFePO4 batteries: experimental analyses of cycling-induced aging, Electrochim. Acta 210 (2016) 445–455, https://doi.org/10.1016/j.electacta.2016.05.091.
[12] J. Groot, M. Swierczynski, A.I. Stan, S.K. Kær, On the complex ageing characteristics of high-power LiFePO4/graphite battery cells cycled with high charge and discharge currents, J. Power Sources 286 (2015) 475–487, https://doi.org/10.1016/j.jpowsour.2015.04.001.
[13] E. Sarasketa-Zabala, F. Aguesse, I. Villarreal, L.M. Rodriguez-Martinez, C.M. López, P. Kubiak, Understanding lithium inventory loss and sudden performance fade in cylindrical cells during cycling with deep-discharge steps, J. Phys. Chem. C 119 (2015) 896–906, https://doi.org/10.1021/jp510071d.
[14] M. Dubarry, C. Truchot, B.Y. Liaw, Synthesize battery degradation modes via a diagnostic and prognostic model, J. Power Sources 219 (2012) 204–216, https://doi.org/10.1016/j.jpowsour.2012.07.016.
[15] M. Dubarry, B.Y. Liaw, Identify capacity fading mechanism in a commercial LiFePO4 cell, J. Power Sources 194 (2009) 541–549, https://doi.org/10.1016/j.jpowsour.2009.05.036.
[16] A.K. Padhi, K.S. Nanjundaswamy, J.B. Goodenough, Phospho-olivines as positive-electrode materials for rechargeable lithium batteries, J. Electrochem. Soc. 144 (1997) 1188–1194, https://doi.org/10.1149/1.1837571.
[17] D. Li, D.L. Danilov, L. Gao, Y. Yang, P.H.L. Notten, Degradation mechanisms of the graphite electrode in C 6 /LiFePO 4 batteries unraveled by a non-destructive approach, J. Electrochem. Soc. 163 (2016) A3016–A3021, https://doi.org/10.1149/2.0821614jes.
[18] M. Schimpe, M.E. von Kuepach, M. Naumann, H.C. Hesse, K. Smith, A. Jossen, Comprehensive modeling of temperature-dependent degradation mechanisms in lithium iron phosphate batteries, J. Electrochem. Soc. 165 (2018) A181–A193, https://doi.org/10.1149/2.1181714jes.
[19] A. Barré, F. Suard, M. Gérard, M. Montaru, D. Riu, Statistical analysis for understanding and predicting battery degradations in real-life electric vehicle use, J. Power Sources 245 (2014) 846–856, https://doi.org/10.1016/j.jpowsour.2013.07.052.
[20] K. Ramirez-Meyers, B. Rawn, J.F. Whitacre, A statistical assessment of the state-of-health of LiFePO4 cells harvested from a hybrid-electric vehicle battery pack, J. Energy Storage 59 (2023), https://doi.org/10.1016/j.est.2022.106472.
[21] G. Sordi, A. Rondi, D. Conti, A. Casalegno, C. Rabissi, Degradation of lithium-ion batteries under automotive-like conditions: aging tests, capacity loss and q-OCP interpretation, Future Batteries 3 (2024) 100005, https://doi.org/10.1016/J.FUB.2024.100005.
[22] G. Sordi, A. Stecchini, R. Evangelista, D. Luder, W. Li, D.U. Sauer, A. Casalegno, C. Rabissi, Degradation of lithium-ion batteries under automotive-like conditions: P2D model-based understanding and ex-situ validation, ETransportation 24 (2025) 100410, https://doi.org/10.1016/j.etran.2025.100410.
[23] A123 Systems, Nanophosphate® High Power Lithium Ion Cell ANR26650M1-A. www.a123systems.com, 2011.
[24] A123 Systems, Nanophosphate® High Power Lithium Ion Cell ANR26650M1-B. www.a123systems.com, 2012.
[25] C. Rabissi, G. Sordi, A. Innocenti, A. Casalegno, Fast and reliable calibration of thermal-physical model of lithium-ion battery: a sensitivity-based method, J. Energy Storage 59 (2023) 106435, https://doi.org/10.1016/J.EST.2022.106435.
[26] G. Sordi, M. Sedzik, A. Casalegno, C. Rabissi, Diagnosis of lithium-ion batteries degradation with P2D model parameters identification: a case study on low temperature charging, Future Batteries 4 (2024) 100006, https://doi.org/10.1016/J.FUB.2024.100006.

[27] C. Rabissi, G. Sordi, A. Innocenti, A. Casalegno, Fast and reliable calibration of thermal-physical model of lithium-ion battery: a sensitivity-based method, J. Energy Storage 59 (2023), https://doi.org/10.1016/j.est.2022.106435.
[28] G. Sordi, D. Luder, W. Li, D.U. Sauer, A. Casalegno, C. Rabissi, Investigation of calendar ageing of lithium-ion battery through physical models with ex-situ validation, J. Power Sources 615 (2024) 235076, https://doi.org/10.1016/J.JPOWSOUR.2024.235076.
[29] J. Chiew, C.S. Chin, W.D. Toh, Z. Gao, J. Jia, C.Z. Zhang, A pseudo three-dimensional electrochemical-thermal model of a cylindrical LiFePO4/graphite battery, Appl. Therm. Eng. 147 (2019) 450–463, https://doi.org/10.1016/j.applthermaleng.2018.10.108.
[30] Y. Huang, H. Lai, Effects of discharge rate on electrochemical and thermal characteristics of LiFePO4/graphite battery, Appl. Therm. Eng. 157 (2019), https://doi.org/10.1016/j.applthermaleng.2019.113744.
[31] J. Li, Y. Cheng, M. Jia, Y. Tang, Y. Lin, Z. Zhang, Y. Liu, An electrochemical-thermal model based on dynamic responses for lithium iron phosphate battery, J. Power Sources 255 (2014) 130–143, https://doi.org/10.1016/j.jpowsour.2014.01.007.
[32] J. Liang, Y. Gan, M. Yao, Y. Li, Numerical analysis of capacity fading for a LiFePO4 battery under different current rates and ambient temperatures☆, Int. J. Heat Mass Transf. 165 (2021) https://doi.org/10.1016/j.ijheatmasstransfer.2020.120615.
[33] L. Zhang, C. Lyu, G. Hinds, L. Wang, W. Luo, J. Zheng, K. Ma, Parameter sensitivity analysis of cylindrical LiFePO 4 battery performance using multi-physics modeling, J. Electrochem. Soc. 161 (2014) A762–A776, https://doi.org/10.1149/2.048405jes.
[34] Y. Huang, H. Lai, Effects of discharge rate on electrochemical and thermal characteristics of LiFePO4/graphite battery, Appl. Therm. Eng. 157 (2019) 113744, https://doi.org/10.1016/J.APPLTHERMALENG.2019.113744.
[35] Y. Ye, Y. Shi, A.A.O. Tay, Electro-thermal cycle life model for lithium iron phosphate battery, J. Power Sources 217 (2012) 509–518, https://doi.org/10.1016/j.jpowsour.2012.06.055.
[36] E. Prada, D. Di Domenico, Y. Creff, J. Bernard, V. Sauvant-Moynot, F. Huet, Simplified electrochemical and thermal model of LiFePO 4 -graphite Li-ion batteries for fast charge applications, J. Electrochem. Soc. 159 (2012) A1508–A1519, https://doi.org/10.1149/2.064209JES/XML.
[37] C. Edouard, M. Petit, C. Forgez, J. Bernard, R. Revel, Parameter sensitivity analysis of a simplified electrochemical and thermal model for Li-ion batteries aging, J. Power Sources 325 (2016) 482–494, https://doi.org/10.1016/j.jpowsour.2016.06.030.
[38] J. Schmalstieg, C. Rahe, M. Ecker, D.U. Sauer, Full cell parameterization of a high-power lithium-ion battery for a physico-chemical model: part I. Physical and electrochemical parameters, J. Electrochem. Soc. 165 (2018) A3799–A3810, https://doi.org/10.1149/2.0321816jes.
[39] J. Ong, J. Newman, Double-layer capacitance in a dual lithium ion insertion cell, J. Electrochem. Soc. 146 (1999) 4360.
[40] M. Park, X. Zhang, M. Chung, G.B. Less, A.M. Sastry, A review of conduction phenomena in Li-ion batteries, J. Power Sources 195 (2010) 7904–7929, https://doi.org/10.1016/j.jpowsour.2010.06.060.
[41] N. Suzuki, Y. Yamashita-Tsukada, N. Hirose, al, N. Wang, Y. Pan, A. Funabiki, M. Lnaba, Z. Ogumi, S. Yuasa, J. Otsuli, A. Tasaka, Impedance Study on the Electrochemical Lithium Intercalation into Natural Graphite Powder, 1998.
[42] D. Carlier, M. Ménétrier, C. Delmas, 7Li MAS NMR study of electrochemically deintercalated LixNi0.30Co0.70O2 phases: evidence of electronic and ionic mobility, and redox processes, J. Mater. Chem. 11 (2001) 594–603, https://doi.org/10.1039/b006179o.
[43] J. Marzec, J.P. Przewoz'nik, J. Molenda, D.R. Simon, E.M. Kelder, J. Schoonman, Conduction mechanism in operating a LiMn_2O_4 cathode, Solid State Ion. 146 (2002) 225–237. www.elsevier.com/locate/ssi.
[44] L.O. Valøen, J.N. Reimers, Transport properties of LiPF[sub 6]-based Li-ion battery electrolytes, J. Electrochem. Soc. 152 (2005) A882, https://doi.org/10.1149/1.1872737.
[45] S.W. Han, Transport and Kinetic Phenomena Linked to Power Performance of Lithium-Ion Batteries, University of Michigan, 2014.
[46] Y.-H. Chen, C.-W. Wang, G. Liu, X.-Y. Song, V.S. Battaglia, A.M. Sastry, Selection of conductive additives in Li-ion battery cathodes, J. Electrochem. Soc. 154 (2007) A978, https://doi.org/10.1149/1.2767839.
[47] Ajit Kumar Dutta, Electrical conductivity of single crystals of graphite, Phys. Rev. 90 (1952).
[48] Comsol, Thermal Modeling of a Cylindrical Lithium-Ion Battery in 2D. www.comsol.com/trademarks, 2021.
[49] Michael Heβ, Kinetics and Stage Transitions of Graphite for lithium-Ion Batteries, ETH Zurich, 2013.